ISSN 3049-7930

Edinburgh Student Journal of Science

Volume 1
Issue 1
July 2024

"The pursuit of science is a grand adventure, driven by curiosity, fueled by passion, and guided by reason"

James Clerk Maxwell

Edinburgh Student Journal of Science

Volume 1

Issue 1

July 2024

ISSN 3049-7930

Published by the University of Edinburgh

Edited and Produced by Jack L Smith

Edinburgh Student Journal of Science

THE UNIVERSITY of EDINBURGH

journals.ed.ac.uk/esjs

Edinburgh Student Journal of Science

Volume 1, Issue 1, June 2024

Cover Illustration

The illustration on the journal cover of each issue is created based on one or more articles from within the issue which the reviewers and editor found to be particularly well-written and engaging.

For this first issue, the cover has been designed to represent the two fields encaptured in the issue: Physics and Geosciences. The design was created with the help of Microsoft Designer, however, in the future we hope to feature artwork from students; if you are interested in designing a future cover, please email us!

Submitting to the Journal

We welcome submissions from later-year undergraduate students within the College of Science and Engineering at the University of Edinburgh. Submissions should be no longer than 1500 words and should summarise work from academic/independent research projects, internships, or summer projects. Full details about submissions criteria and guidelines can be found on our website.

The Edinburgh Student Journal of Science is a student-run peer-reviewed journal for later year undergraduate students studying science at the University of Edinburgh. It is an opportunity for students to publish summaries of their academic or independent research in a professional-style journal and get a feel for the publishing and peer-review processes.

The journal is issued every four months to coincide with the end of both academic semesters for academic projects and Bachelor's/Master's theses, and the end of the Summer break for Summer projects or internships.

The next issue of the Edinburgh Student Journal of Science is expected to be published in October with a deadline for submissions in September. For more information, templates, and guidance on submitting an article, find more details on our website: journals.ed.ac.uk/esjs.

If you have feedback on any of the articles featured in this issue, or on this issue as a whole, feel free to submit your comments or thoughts by emailing ESJS@ed.ac.uk. If you have specific comments or feedback on a particular article, their ORCID IDs should be consulted in the first instance, but your notes can be sent to the authors of the article at your request (and at the discretion of the editors).

Contents

Physics and Astronomy

Geosciences

Physics and Astronomy

Adding a Vorticity Source to the Hasegawa-Wakatani Equations

Shae Tjong*[1], Robin Varennes[2]

[1] School of Physics and Astronomy, University of Edinburgh
[2] Nanyang Technological University, Singapore

Open Access

Received
15 May 2024

Revised
24 May 2024

Accepted
29 May 2024

Published
04 Jul 2024

Abstract

Instabilities in fusion reactor plasma are an area of ongoing research as they represent the primary hurdle in producing an ongoing fusion reaction for fusion energy production. To study one possible source of these instabilities, computational simulations to solve the modified Hasegawa-Wakatani Equations and the evolution of edge plasmas through time are required. This work shows that the addition of a source of vortices leads to edge instabilities using the TOKAM2D turbulence code. This is an important step into developing our understanding of how instabilities form in plasmas and maintaining a fusion reaction.

DOI: 10.2218/esjs.9671 **ISSN** 3049-7930

Introduction

Tokamak fusion reactors are a type of fusion reactor which includes the largest planned test reactor in France (Tomabechi *et al.* 1991). Such reactors are torus-shaped devices which use electrical and magnetic confinement to contain a high-temperature plasma where nuclear fusion reactions can take place. A problem in Tokamak reactors is the emergence of turbulences; one source of instabilities that leads to turbulence is the edge plasma, plasma near the outer radius of the torus which is susceptible to edge effects. The region where edge plasmas are relevant is known as the Scrape-Off Layer (SOL).

Method

The Hasegawa-Wakatani (HW) equations are the set of 2D differential equations describing the evolution of the potential and density of edge plasmas in the SOL of Tokamak reactors. This research used the modified Hasegawa-Wakatani (mHW) system, where only local deviations from the average are studied, to investigate the effects of adding an extra vorticity term:

$$\frac{\partial \hat{N}}{\partial t} + \kappa \frac{\partial \hat{\phi}}{\partial y} + \{\hat{\phi}, \hat{N}\} - D\nabla^2 \hat{N} = S + C(\hat{\phi} - \hat{N}), \tag{1}$$

$$\frac{\partial \hat{V}}{\partial t} + g\frac{\partial \hat{N}}{\partial y} + \{\hat{\phi}, \hat{V}\} - D\nabla^2 \hat{V} = C(\hat{\phi} - \hat{N}) - \nu(V - V_0). \tag{2}$$

*Student Author

where N is the number density of charged particles, ϕ is the matter potential, vorticity is $V = \nabla^2\phi$, and $\{x, y\}$ is the standard Poisson bracket. The presence of a $\hat{}$ indicates the use of the local deviation from the average, for example, $\hat{N} = N - \langle N \rangle$, which is not present in the HW system. The parameters g, D, S, and C are all fixed as $g = S = 0$, $D = 10^{-3}$, and $C = 2$, using the computational unit basis. These parameters determine the strength of each term which act as sources or sinks term and are related to the physical properties of the plasma. This project investigated the effect of adding the term $(V - V_0)$ which forces the vorticity of the plasma towards a predetermined value V_0. ν acts as a parameter which controls the strength of this forcing. The mHW system is used because vorticity is a periodic, local phenomenon.

To simulate the evolution of instabilities in Tokamak edge plasmas, the turbulence code TOKAM2D (Sarazin *et al.* 2003) was used to numerically solves the HW system (Hasegawa *et al.* 1983), with modifications to solve the mHW system made by Dr. R. Varennes. To check the evolution of the plasmas were physically reasonable, animations of the density, potential, and vorticity were generated.

To investigate how the plasma density flux behaves with the addition of this term, the parameter ν was varied. It was found that negative values resulted in immediate numerical crashes. It was also found that values above 0.3 would result in numerical crashes which occurred so rapidly that no usable data could be collected. These crashes are a result of calculating nonphysical magnitudes in the potential or density of the plasma which could not arise in a Tokamak reactor. To obtain the results shown in Section 2, ν in the range $[0.00, 0.10]$ in steps of 0.005 was used. For greater values of ν, it could be concluded that numerical noise was skewing the data enough that simulations with such values must be discounted.

The form of V_0 was required to be periodic because TOKAM2D uses Fourier transformations to solve partial differential equations. Two forms for V_0 were simulated, one with V_0 as a sinusoidal function and one with $V_0 = 10$, with $\kappa = 0$. These forms were chosen as they are not computationally difficult to calculate and allowed for rapid simulations. A third set of simulations was carried out with $V_0 = 10$ and $\kappa = 1$ to compare the results of adding a vorticity source with the results generated without a vorticity source (Heinonen *et al.* 2020), with modifications in the code to match the simulations of previous research. In the case of $\kappa \neq 0$, this physically corresponds to a set of imposed gradients in plasma density which act as sources of instabilities. Time was measured as the number of periodic cycles of plasma in the Tokamak and each simulation was run for a maximum of 4800 periods. To carry out these simulations the HPCC Wildfly Supercomputing Cluster was used.

Due to the aforementioned Fourier transforms in TOKAM2D, care had to be taken in choosing the time steps used. As ν was increased, the speed at which instabilities arose increased, leading to progressively decreasing simulation times before crashes occurred. Preceding a numerical crash, the density flux rapidly increased in a manner which could potentially skew the data and to take this into account, data immediately before these rapid increases were discounted. Data before plasma instabilities were discounted to avoid skewing the results due to some simulations having longer or shorter stable phases.

Since the simulations were over a region within the SOL, the sum of the vertically averaged density flux over the whole region was used as a measure of the instability as this is the net material flux of the plasma in the SOL. This was plotted to determine how much of the data gathered in each simulation was reasonable and how much had to be discounted. The analysis of these plots and the determination of the start of the instability phase and the beginning of numerical errors was done by manual inspection of each plot. As the fluctuations were centred around zero, the average of the root-mean-square (RMS) of the fluctuations was used to study the behaviour of the density flux.

Results

Across all simulations, it was found that the RMS of the density flux increased to a local maximum at $\nu = 0.025$ (for sinusoidal V_0 and constant V_0 with $\kappa = 1$) or $\nu = 0.030$ (for constant V_0 with $\kappa = 0$) before decreasing to a local minimum at $\nu = 0.065$ or $\nu = 0.070$, respectively. Plots of these data are shown in Figure 1.

The general shape of the plots was consistent across all simulations including a linear decrease between the local maximum and minimum. A notable discrepancy was the density flux for $\nu = 0$ and $\nu = 0.005$. In the case shown for constant V_0, the density flux is initially 0. However, in the case for $V_0 = 10$ and $\kappa = 1$, the initial values were comparable to when $\nu = 0.03$.

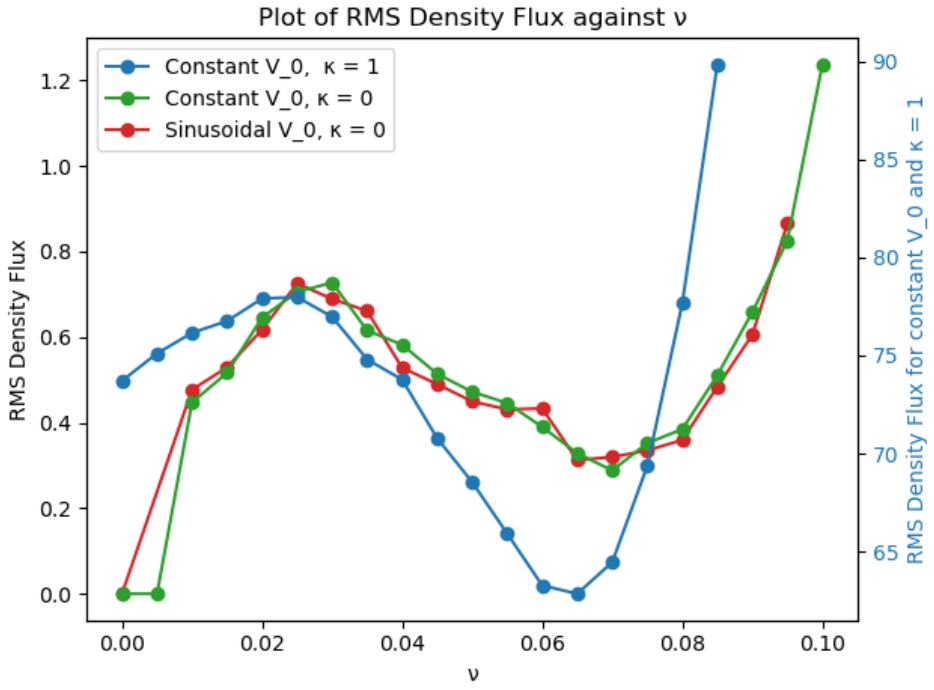

Figure 1: Plot of RMS Density flux against ν with scales for $\kappa = 0$ on the left and $\kappa = 1$ on the right. RMS was calculated from the onset of instabilities and ending before numerical crashes occurred or after 4800 time periods elapsed. All values are given in the computational unit basis.

Analysis and Interpretation

The matching shapes of the graphs for each simulation suggest that a physically relevant effect occurs when the vorticities of edge plasmas are forced towards a certain value. Furthermore, when using comparable parameters, these individual graphs of density flux agree with previous published research (Ghendrih *et al.* 2022) without vorticity sources, as expected. Where there is no density flux, there may be some threshold value below which stabilising elements overcome the destabilising effects of adding a vorticity source.

It is possible to attribute the decrease between the local maximum and minimum to the development of mean velocity shears which have a stabilising effect on the instabilities in the plasma; however, such shears were not visible in the animations generated by the code. Whether this is due to the resolution of the animations being too low or due to a lack of stabilising shears in the simulation is yet to be determined. Following the local minimum, rapid increases in density flux are observed in all simulations. This may be due to the growing effect of numerical errors, though alternatively, it may be due to Kelvin-Helmholtz instabilities arising when mean velocity shears grow too large, studying this behaviour should be the focus of future research.

Conclusion

This work investigated the effects adding a source of vorticity to the modified Hasegawa-Wakatani equations. It was shown that for a variety of vorticity sources, instabilities in the Scrape-Off Layer in Tokamak edge plasmas are produced. This novel result clearly indicates that vortices are a relevant source of instabilities which can cause fusion reactions to fail.

Further research should determine the exact nature of the instabilities formed and whether they can be attributed to mean velocity shear. Work going forward should attempt to extend the number of periods simulated by varying the time step and number of calculations per time step for each value of ν. Additionally, attempts should be made to determine the exact conditions for ν which will result in instabilities by analytically analysing the mHW system. Such work could potentially show us how to

maintain an ongoing fusion reaction and unlock the potential that such an achievement possesses.

Acknowledgements

This research is supported by the National Research Foundation, Singapore. The author wishes to acknowledge the support of Prof. Xavier Garbet and Prof. Qu ZhiSong without whose help this research would not have been possible.

References

Ghendrih, P. *et al.* 'Role of Avalanche Transport in Competing Drift Wave and Interchange Turbulence' in Journal of Physics: Conference Series **2397** 1 (IOP Publishing; 2022)

Hasegawa, A. and Wakatani, M. 'Plasma Edge Turbulence' Physical Review Letters **50** 9 (1983)

Heinonen, R. A. and Diamond, P. H. 'Learning How Structures Form in Drift-Wave Turbulence' Plasma Physics and Controlled Fusion **62** 10 (2020)

Sarazin, Y *et al.* 'Theoretical Understanding of Turbulent Transport in the SOL' Journal of Nuclear Materials **313** (2003)

Tomabechi, K. *et al.* 'ITER Conceptual Design' Nuclear Fusion **31** 6 (1991)

Peering into the Cosmic Dawn: JWST Cycle 1 Data Reveals Early Galaxy Candidates at Redshifts z > 9.5

Maja Seweryna Zielinska*[1]

[1] School of Physics and Astronomy, University of Edinburgh

Open Access

Received
23 May 2024

Revised
11 Jun 2024

Accepted
12 Jun 2024

Published
04 Jul 2024

Abstract

Observing high-redshift objects provides a window into the past, enabling insight into galaxy formation, matter distribution, and the nature of dark matter and energy. This report presents a sample of work on Cycle 1 of the James Webb Space Telescope concerning the discovery of high-redshift early galaxy candidates. Potential objects from these surveys had their photometric redshift computed using the LePhare simulation program and analysed using LePhare-generated spectral energy distribution fits. A total of 46 candidates at redshifts beyond $z > 9.5$ were found between three surveys: two in DDT2750, 30 in JADES, and 14 in NGDEEP.

DOI: 10.2218/esjs.9673 **ISSN** 3049-7930

Introduction

The search for high-redshift galaxies comes from a desire to know more about the early universe; these galaxies appear now as they were in the past. Their structure, metallicity, and dynamics can give insight into how galaxy formation and evolution has changed with time. The development of better instruments and further constraint of cosmological constants has led to redshift determination of sources further and further back in time.

Due to the high number of foreground interlopers, the techniques used to select only high-redshift galaxies need to be specific. One of the most effective is the selection of galaxies via the Lyman break – a distinct "step" in the blue side of the spectrum, where the majority of ultraviolet (UV) light from young stars has been absorbed by neutral interstellar hydrogen gas (Dunlop 2013). With the combined effect of the Lyman-α forest at higher redshifts (from Lyman-α absorption at $\lambda_{rest} = 1216$Å), the optical thickness becomes so great that only a sharp-edged "step" in the spectrum remains.

It is possible to select high-redshift galaxies by viewing candidate objects through different filters and seeing in which one an object "drops out" – the object should be repeatedly visible in all longer wavelengths, but no longer so at the bluest wavelengths. The filter in which the object "disappears" will correlate to the redshift at which it lies, as it will relate to how much the Lyman break has been shifted along with the spectrum. This technique has successfully been utilised on early-release James Webb Space Telescope (JWST) data, resulting in a multitude of high-probability candidates (Donnan *et al.* 2022; Harikane *et al.* 2023). Given this result, the same technique was utilised in this project.

The JWST data for this report was taken from three separate surveys – DDT2750, JADES, and NGDEEP – with each survey focused on a different area of the sky, and utilising a different filter set for observations. JADES in particular was highly anticipated; instruments used as part of this survey allowed an unprecedented extension of imaging into the infrared spectrum. JADES was the largest survey included in this report, lying in the footprints of the Hubble Deep Field and the Hubble Ultra Deep Field (JADES 2023). All filters used as part of this project can be found in the JWST and Hubble Space Telescope User Documentation (HST 2020; JWST 2023). The filters used for each survey were different and had different wavelength overlap regions[†].

*Student Author

[†]DDT2750 utilised filters F115w, F150w, F200w, F277w, F356w, F444w. JADES utilised F435w, F606w, F814w, F090w, F115w, F150w, F200w, F277w, F356w, F410m, F444w. NGDEEP used F435w, F606w, F814w, F115w, F150w,

Methods

Catalogues

SourceExtractor is a command-line program which analyses large-scale astronomical files and is able to reduce and compile catalogues of potential sources from said data (Bertin *et al.* 1996). By running SourceExtractor in dual image mode, it was possible to make detections in one image and use those object coordinates to make measurements in a second image. Hence, the F277w filter image was used as the detection image for each dataset, allowing for the creation of catalogues. This specific filter was chosen as it was well-populated across all three surveys.

Each catalogue contained the object identification number, coordinates, object flux, and flux error; these separate filter catalogues were assembled into one master catalogue per survey. The compiled catalogues were cut to select for desired objects – only those detected at 5σ over the noise in F277w would be selected, and were subjected to a secondary non-detection cut in F115w and F090w as a final step. These cuts ensured that the objects that remained in the catalogues statistically fulfilled the criteria for detection.

These reduced catalogues could then be input into the LePhare program. LePhare is a set of Fortran commands that compute an object's photometric redshift and perform spectral energy distribution (SED) fitting on datasets, using galactic models from its libraries (Arnouts *et al.* 2011). The LePhare output totalled thousands of objects and had to be sorted for the desired outcome. Objects were selected between redshifts of $9.5 < z < 16$; any higher than 16 was anticipated to be noise. Objects were then cut at the statistical hypothesis value of $\chi^2 < 50$.

Even after this selection, the number of total objects remained very high. It was improbable that so many high redshift galaxies would be present – more likely that some of the candidates were false positives. A more selective cut was performed in F277w, seeking any objects 8σ above the noise in comparison to the 5σ selection chosen before. These catalogue cuts yielded a manageable sample of objects that could be visually assessed to select high-redshift candidates via the postage stamp method.

Postage Stamps

A reduced catalogue with just the high-redshift objects was created for each survey, containing the object coordinates in each image. From this, individual "stamps" were made by centering the identified object in each image cutout for each filter.

High-redshift, star-forming objects such as early galaxies were expected to only be visible at longer wavelengths due to the Lyman break. As different filters cover a different waveband, only certain wavelengths of light can be seen in each image; the filter in which the object "drops out" correlates to the expected redshift value. An example of a successful object detection can be seen in the "post-stamp" set in Figure 1. Any "post-stamp" set with this dropout criteria had the object number noted down, and these chosen objects were re-run through LePhare to obtain primary and secondary SED fits.

Results and Discussion

The primary solution created by LePhare simulated a spectrum of a high-redshift galaxy projected at the same redshift as the solution found for the object. The secondary solution posited a galaxy at a much lower redshift but with a very red ('dusty') spectrum to make it appear more redshifted. The object's magnitude and wavelength values could be compared for reference.

For many of the objects, there was no secondary solution in the initial run – a sign of a very good primary fit, or that LePhare did not project a secondary fit. To gain a secondary low-redshift fit to compare the primary solution to, a second run of objects was input into LePhare with changed solution parameters to force a low-redshift outcome. From analysis by eye of the postage stamps and subsequent comparison to SED fits drawn up of the object, a total of two candidate objects were found in the DDT2750 survey, 30 in JADES, and 14 in NGDEEP. All these are projected to lie at redshifts beyond $z = 9.5$.

The next step for this research would be to look at the UV luminosity density and the Star Formation Rate Densities of these galaxies. These sorts of results can be added to and compared to previous studies

F200w, F277w, F356w, F444w. Filters F606w, F814w are from ancillary HST surveys (Baggett *et al.* 2006; HST 2020).

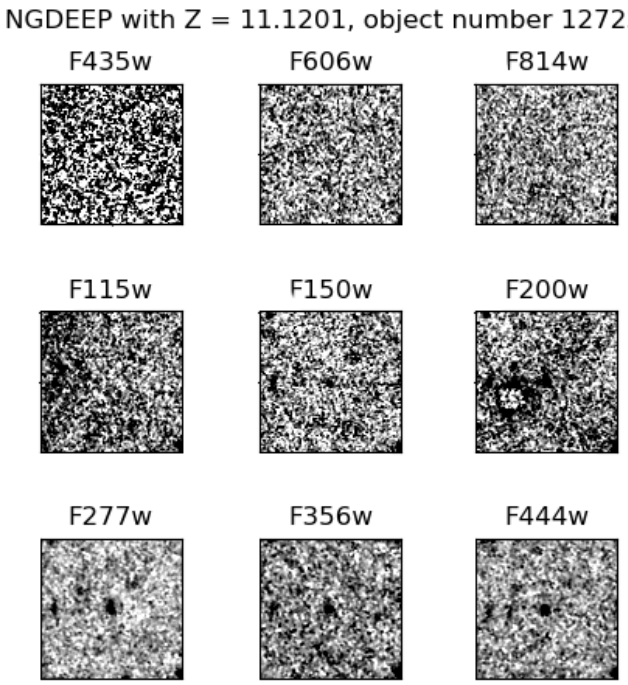

Figure 1: Cutouts of the NGDEEP object 12723. The object is visible as a black dot at centre of each image cutout in filters used at longer wavelengths (F150w-F444w), while disappearing from shorter-wavelength observations (F435w-F115w) due to the Lyman break. This demonstrates the criteria necessary to visually identify a potential high-redshift candidate by the method of "postage stamps".

to further support or disprove existing relations, and ultimately yield a better picture of the early universe (Donnan *et al.* 2022).

For a first foray into the high-redshift regime, this project served as a good introduction to the processes involved in handling high-redshift data. The results suggest the existence of candidates at z-values much higher than records set prior to the launch of the JWST (Oesch *et al.* 2016; Jiang *et al.* 2020). If confirmed spectroscopically, these candidates could very well be some of the first galaxies formed in our universe.

Acknowledgements

I would like to thank Dr. Derek McLeod, my project supervisor, for the invaluable support and assistance that was extended to me. I express my sincere appreciation to the journal editors and reviewers for their comments and constructive feedback. This project was made possible and funded by the Edinburgh University School of Physics and Astronomy Career Development Summer Scholarship. Observations were made with the NASA/ESA Hubble Space Telescope (Whitaker *et al.* 2019) and the NASA/ESA/CSA James Webb Space Telescope (Bunker *et al.* 2023; Eisenstein *et al.* 2023; Rieke *et al.* 2023a,b; Bagley *et al.* 2024).

References

Arnouts, S. and Ilbert, O. 'LePHARE: Photometric Analysis for Redshift Estimate' Astrophysics Source Code Library (2011)

Baggett, S *et al.* 'Filters for HST Wide Field Camera 3' in Space Telescopes and Instrumentation I: Optical, Infrared, and Millimeter **6265** (Society of Photo-Optical Instrumentation Engineers; 2006)

Bagley, M. B. *et al.* 'The Next Generation Deep Extragalactic Exploratory Public (NGDEEP) Survey' The Astrophysical Journal Letters **965** 1 (2024)

Bertin, E. and Arnouts, S. 'SExtractor: Software for Source Extraction' Astronomy and Astrophysics Supplement Series **117** 2 (1996)

Bunker, A. J. *et al.* 'JADES NIRSpec Initial Data Release for the Hubble Ultra Deep Field: Redshifts and Line Fluxes of Distant Galaxies From the Deepest JWST Cycle 1 NIRSpec Multi-object Spectroscopy' arXiv e-prints (2023)

Donnan, C. T. *et al.* 'The Evolution of the Galaxy UV Luminosity Function at Redshifts Z $\simeq$ 8 –15 From Deep JWST and Ground-Based Near-Infrared Imaging' Monthly Notices of the Royal Astronomical Society **518** 4 (2022)

Dunlop, J. S. 'Observing the First Galaxies' in The First Galaxies **396** (Springer Berlin Heidelberg; 2013)

Eisenstein, D. J. *et al.* 'Overview of the JWST Advanced Deep Extragalactic Survey (JADES)' arXiv e-prints (2023)

Harikane, Y. *et al.* 'A Comprehensive Study of Galaxies at Z $\sim$ 9–16 Found in the Early JWST Data: Ultraviolet Luminosity Functions and Cosmic Star Formation History at the Pre-reionization Epoch' The Astrophysical Journal Supplement Series **265** 1 (2023)

HST 'WFC3 Filter Throughputs' *Accessed 24th Sep 2023* (2020)

JADES 'JWST Advanced Deep Extragalactic Survey' *Accessed 11th Sep 2023* (2023)

Jiang, L. *et al.* 'Evidence for GN-z11 as a Luminous Galaxy at Redshift 10.957' Nature Astronomy **5** 3 (2020)

JWST 'NIRCam Filters' *Accessed 11th Sep 2023* (2023)

Oesch, P. A. *et al.* 'A Remarkably Luminous Galaxy at Z = 11.1 Measured With Hubble Space Elescope GRISM Spectroscopy' The Astrophysical Journal **819** 2 (2016)

Rieke, M. *et al.* 'Data From the JWST Advanced Deep Extragalactic Survey (JADES)' Mikulski Archive for Space Telescopes (2023)

Rieke, M. *et al.* 'JADES Initial Data Release for the Hubble Ultra Deep Field: Revealing the Faint Infrared Sky With Deep JWST NIRCam Imaging' Astrophysical Journal Supplement Series **269** 1 (2023)

Whitaker, K. E. *et al.* 'The Hubble Legacy Field GOODS-S Photometric Catalog' The Astrophysical Journal Supplement Series **244** 1 (2019)

Performing Automated, High-Speed Photometry on Occulting, Small Outer Solar System Bodies

Ben Mark Attwood*[1], James E. Robinson[1]

[1] School of Physics and Astronomy, University of Edinburgh

Open Access

Received
24 May 2024

Revised
14 Jun 2024

Accepted
24 Jun 2024

Published
04 Jul 2024

Abstract

Monitoring stellar occultations provides a powerful means to measure the shapes and sizes of small Solar System bodies, but produces large quantities of image data which can be laborious to analyse. An automated Python-based software, `occ_find`, was written for performing high-speed aperture photometry on `spool` files packed with large volumes of images from the 1.54m Danish Telescope. `occ_find` processed 11 `spool` files at a maximum rate of around 4-6 minutes per `spool` file, without image reduction. From these files, 3 occultation events were detected. The measured chord lengths are consistent with prior size measurements of these small bodies.

DOI: 10.2218/esjs.9682 **ISSN** 3049-7930

Introduction

Of the many small bodies that exist in the Solar System, there is an enormous variety in their shapes and sizes, and there exists a plethora of methods for measuring them, as well as looking for the presence of rings and/or satellites. Such methods include spacecraft visits, radar observations, and lightcurve shape modelling; that is using changes in the brightness of the body with time to model its approximate shape (Kaasalainen *et al.* 2001a,b).

Stellar occultation events provide another means of measuring the shapes and sizes of small bodies. A stellar occultation is where a small body within the Solar System passes through the line of sight to a background star, causing it to be blocked momentarily. Since the stars are significantly further from the observer than the occulting body, the rays of light emitted can be approximated as parallel. Therefore, the shadow the body casts on the Earth will be the same size and shape as the body. By measuring the duration of the occultation, t_{occ}, and the orbital speed of the body relative to Earth, v_{rel}, the length of the occulting body in the direction of travel at a particular point on the Earth – referred to as the 'chord' of the occultation, l_{chord} – can be calculated:

$$l_{\text{chord}} = v_{\text{rel}} t_{\text{occ}} \tag{3}$$

Measuring at least 3 well separated chords (that is, the chords are measured from points on the Earth with sufficiently different latitudes) sampling the same aspect of the body is sufficient to determine it's size assuming an ellipsoidal shape, true of large Trans-Neptunian Objects (TNOs) and dwarf planets. Furthermore, multiple chords allow us to accurately constrain the shape of smaller, more irregular bodies such as (486958) Arrokoth (Lissauer *et al.* 2019; Buie *et al.* 2020).

Stellar occultation measurements have led to several major Solar System discoveries such as the discovery of ring systems around the planets Uranus and Neptune (Elliot *et al.* 1977; Reitsema *et al.* 1981), and more recently, the centaur (a type of small body inhabiting the region between the orbits of Jupiter and Neptune) (10199) Chariklo, along with numerous other small bodies since then (Braga-Ribas *et al.* 2014; Ortiz *et al.* 2017; Pereira *et al.* 2023). Occultation measurements also revealed the presence of

*Student Author

the Neptunian satellite Larissa (Hubbard *et al.* 1986), its existence later confirmed by Voyager 2 (Smith *et al.* 1989).

Monitoring stellar occultation events presents a number of technical challenges – rapid imaging (10 Hz frame rate in this work) of the target star is required to accurately capture the drop-off in stellar flux, resulting in a large volume of image data ($\sim 10^3$ images or $\sim$1 GB of data for a typical observation). Because of this, without some sort of automation: analysis of these images is a very laborious and time-consuming task. Furthermore, due to uncertainty in the predicted size, shape, and path of the body, there is no way to guarantee in advance that an occultation will be observed at a particular location on the Earth. Therefore, a set of images from an observation is not guaranteed to yield a chord.

Automated photometric pipelines provide a convenient solution to some of these challenges (Assafin *et al.* 2011; Anderson 2019; Pavlov 2020). These pipelines allow for rapid processing and analysis of image data, which provides a tool for the observer to determine whether or not an occultation was detected immediately after an observation is made. Furthermore, this allows for quick identification of occultation events from large archives of observational data spanning many years. The processed data can then be used to assist the efforts of groups monitoring occultation events (LESIA 2022; IOTA 2024).

In this work, I wrote a Python software package called `occ_find` to extract and analyse image data from an archive of `spool` files taken by the Lucky Star Project using the Two Colour Instrument (TCI) on the 1.54m Danish Telescope at La Silla, Chile. The TCI supplies HDF5 (Hierarchical Data Format) `spool` files containing image data. HDF5 is a compact data file format allowing storage of large volumes of image data (and associated metadata) from each observation. Following extraction, aperture photometry – the measurement of flux from a source within a fixed region of the image – was performed on all detected stars in each image. The software returns a lightcurve, a plot of the stellar flux against time, for each star in the images. The lightcurves can be manually inspected for occultation events (see Results and Analysis section). The lightcurves, photometry, and time data was also saved in multiple formats to enable further processing by the user if required. `occ_find` was tested on an archive of 11 `spool` files, and the chord lengths calculated from any detected occultation events were compared with past size measurements of the target bodies.

Methods

The `occ_find` package consists of three Python scripts:

1. `h5_unpack` – for extraction and conversion of datasets from the HDF5 file to either `.fits` (image data) or `.txt` (metadata) file format.
2. `reducto` – for image reduction to account for instrumental errors and biases; optional, see below.
3. `occ_find` – for detecting stars in the images and plotting their lightcurves.

The HDF5 `spool` files must first be unpacked for analysis; when `h5_unpack` is called, the files are saved into a `spool` directory, with all image data saved into its own sub-directory called `images`. At this point, the software `reducto` can be called to perform image reduction using bias and flat-field images supplied within the `spool` files, if required. Image reduction with `reducto` is not essential if the user simply wishes to process a large archive to quickly find occultation events, however, reduction is recommended if any further analyses are to be performed. `occ_find` opens the first `.fits` image from the `spool` and uses a star-finding routine to detect the sources within it (Bradley *et al.* 2023). If sources are found, `occ_find` proceeds to perform aperture photometry at their pixel coordinates in every `.fits` image extracted from the `spool` file, recording the photometry results in a `.txt` file. Finally, the lightcurves are plotted from this data and the time data (extracted from the `spool` file by `h5_unpack`).

Results and Analysis

11 `spool` files (with a typical size of $\sim$1.5 GB) were processed using the `occ_find` package on a Dell Latitude E7450 laptop with an Intel i5-3500 processor. 3 occultation events were detected from the TNOs: (278361) 2007 JJ_{43}, (28978) Ixion, and (120347) Salacia. Their lightcurves, as shown in Figures 1a-c, display a very sharp drop in stellar flux during the occultation, unlike a null result as shown in Figure 1d. In Figure 1d, the variation in stellar flux is due to changing observing conditions. The

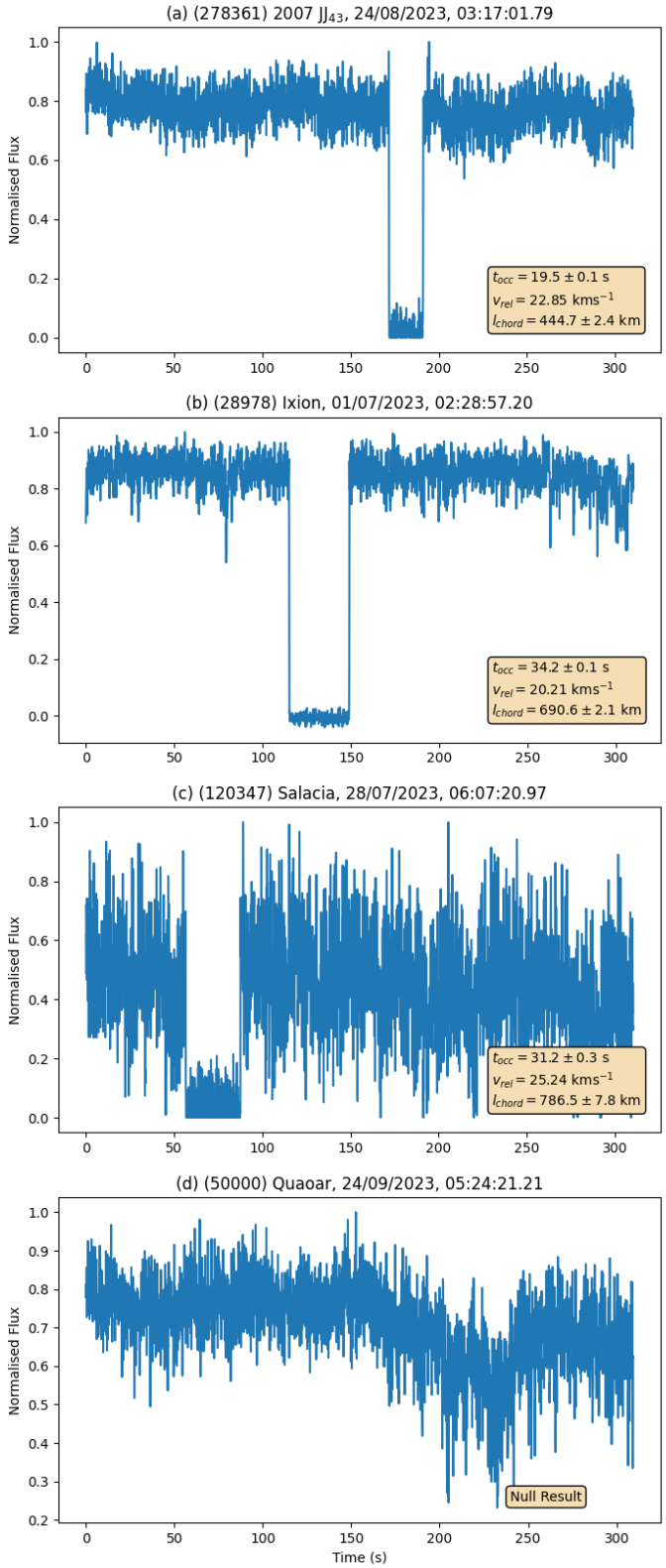

Figure 1: Lightcurves with date and start time of the observation, in UTC, for: **(a)** (278361) 2007 JJ_{43}, **(b)** (28978) Ixion, **(c)** (120347) Salacia, and **(d)** no occultation event (the occulting body targeted was (50000) Quaoar). The relative velocities are taken from the predictions for each event (Lucky Star Project 2023a,b,c).

chord lengths of these bodies calculated using equation (3), and the relative velocity predictions for these events (Lucky Star Project 2023a,b,c), are between 400 and 800 km. This is consistent with prior size measurements of these bodies in literature (Barry *et al.* 2015; Pál *et al.* 2015; Brown *et al.* 2017; Grundy *et al.* 2019; Rommel *et al.* 2020; Levine *et al.* 2021).

The total runtime of the code was on average, ∼4-6 minutes per `spool` file, without image reduction. Adding image reduction increased the runtime by a factor of ∼3, but reduction is not essential for detecting occultations given the significant drop in flux during an event. Without automation, measuring the fluxes of each star in each image using a software such as GAIA (Currie *et al.* 2014) would be prohibitively laborious.

`occ_find` does possess some limitations – it cannot account for any telescope movement throughout the course of the observation (e.g "dither"), which may lead to inaccuracies in the photometry, nor is it well optimised for detecting fainter sources or poor observing conditions, leading to false source detection amongst background noise. Fortunately, false sources are easily distinguished from true lightcurves and occultation events by manual inspection.

Conclusions

Overall, the code allows for rapid processing of large archives of `spool` files to find occultation events, though there are some limitations and scope for improvement. Future work will include updating the code to account for false sources, telescope dither, and to remove null-results. Furthermore, I aim to test of the software on a wider range of `spool` files to further analyse it's performance. In summary, `occ_find`, and photometric pipelines like it, yield the opportunity to monitor occultation events, accurately measure the shapes and sizes of many small bodies, and build a better understanding of their size and shape distribution throughout the Solar System as a whole.

Acknowledgements

This work was undertaken as a senior honours project for the author's BSc (Hons) Astrophysics degree at the University of Edinburgh School of Physics and Astronomy. The author is grateful to Prof. Colin Snodgrass and Dr. Jamie Robinson for supplying the numerous `spool` files from the Danish Telescope for analysis, and their support and encouragement throughout the project.

This work made use of Photutils, an Astropy package for detection and photometry of astronomical sources (Bradley *et al.* 2023).

Software Availability

The code written for this project is available at: `https://github.com/BenAttwood449/occ_find.git`.

References

Anderson, B. 'PyMovie - A Stellar-Occultation Aperture-Photometry Program' Journal for Occultation Astronomy **9** 4 (2019)

Assafin, M. *et al.* 'PRAIA - Platform for Reduction of Astronomical Images Automatically' in Proceedings of Gaia Follow-up Network for Solar System Objects Workshop held at IMCCE-Paris Observatory (2011)

Barry, M. A. *et al.* 'A Digital Video System for Observing and Recording Occultations' Publications of the Astronomical Society of Australia **32** (2015)

Bradley, L. *et al.* 'astropy/Photutils' Zenodo (2023)

Braga-Ribas, F. *et al.* 'A Ring System Detected Around the Centaur (10199) Chariklo' Nature **508** 7494 (2014)

Brown, M. E. and Butler, B. J. 'The Density of Mid-sized Kuiper Belt Objects From ALMA Thermal Observations' The Astronomical Journal **154** 1 (2017)

Buie, M. W. *et al.* 'Size and Shape Constraints of (486958) Arrokoth From Stellar Occultations' The Astronomical Journal **159** 4 (2020)

Currie, M. J. *et al.* 'Starlink Software in 2013' in Astronomical Data Analysis Software and Systems XXIII **485** (Astronomical Society of the Pacific Conference Series; 2014)
Elliot, J. *et al.* 'Occultation of SAO 158687 by Uranian Satellite Belt' IAU Circular **3051** (1977)
Grundy, W. M. *et al.* 'Mutual Orbit Orientations of Trans-neptunian Binaries' Icarus **334** (2019)
Hubbard, W. B. *et al.* 'Occultation Detection of a Neptunian Ring-Like Arc' Nature **319** 6055 (1986)
IOTA 'International Occultation Timing Association' *Accessed 24th May 2024* (2024)
Kaasalainen, M. and Torppa, J. 'Optimization Methods for Asteroid Lightcurve Inversion: I. Shape Determination' Icarus **153** 1 (2001)
Kaasalainen, M. *et al.* 'Optimization Methods for Asteroid Lightcurve Inversion: II. The Complete Inverse Problem' Icarus **153** 1 (2001)
LESIA 'ERC Lucky Star Project' *Accessed 24th May 2024* (2022)
Levine, S. E. *et al.* 'Occultation of a Large Star by the Large Plutino (28978) Ixion on 2020 October 13 UTC' The Astronomical Journal **161** 5 (2021)
Lissauer, J. J. and de Pater, I. 'Fundamental Planetary Science, Updated Edition' (Cambridge University Press; 2019)
Lucky Star Project 'Occultation by 2007JJ43 (2023-07-01)' *Accessed 26th Mar 2024* (2023)
Lucky Star Project 'Occultation by Ixion (2023-07-28)' *Accessed 26th Mar 2024* (2023)
Lucky Star Project 'Occultation by Salacia (2023-09-24)' *Accessed 26th Mar 2024* (2023)
Ortiz, J. L. *et al.* 'The Size, Shape, Density and Ring of the Dwarf Planet Haumea From a Stellar Occultation' Nature **550** 7675 (2017)
Pál, A *et al.* 'Pushing the Limits: K2 Observations of the Trans-neptunian Objects 2002 GV_{31} and (278361) 2007 JJ_{43}' The Astrophysical Journal Letters **804** 2 (2015)
Pavlov, H. 'Tangra: Software for Video Photometry and Astrometry' Astrophysics Source Code Library (2020)
Pereira, C. L. *et al.* 'The Two Rings of (50000) Quaoar' Astronomy & Astrophysics **673** (2023)
Reitsema, H. J. *et al.* 'Discovery of a Probable Third Satellite of Neptune' in Bulletin of the American Astronomical Society **13** (AAS Publishing; 1981)
Rommel, F. L *et al.* 'Stellar Occultations Enable Milliarcsecond Astrometry for Trans-neptunian Objects and Centaurs' Astronomy & Astrophysics **644** (2020)
Smith, B. A. *et al.* 'Voyager 2 at Neptune: Imaging Science Results' Science **246** 4936 (1989)

Geosciences

Assessing the Reliability of Early Marine Cements in Recording Changes in Seawater Redox Conditions Across the Late-Devonian Mass Extinction

Craig Mellon*[1], Rachel Wood†[1], Laetitia Pichevin[1]

[1] School of Geosciences, University of Edinburgh

Open Access

Received
24 May 2024

Revised
08 Jun 2024

Accepted
11 Jun 2024

Published
04 Jul 2024

Abstract

The Late-Devonian Mass Extinction (LDME) extinguished up to 40% of all marine species, with evidence suggesting marine anoxia was the primary cause. This study performs rare earth element analysis of early marine cements from reefal limestones from Australia and Scotland to show that these cements capture a marine anoxic signature across the LDME for the first time, directly implicating marine anoxia and by extension, the rise of land plants, as the cause of the LDME. This work also demonstrates that early marine cements serve as reliable proxies for recording changes in seawater redox conditions over whole-rock analysis.

DOI: 10.2218/esjs.9681 **ISSN** 3049-7930

Introduction and Motivation

The Late-Devonian Mass Extinction (LDME) is one of the "big 5" mass extinctions (Raup *et al.* 1982) and occurred approximately 371.9 million years ago (Ma) (Racki 2021). The extinction event lasted roughly 1 million years (Myr) and, uniquely, was characterised by up to 5 "bursts" of species death, each of varying severity (McGhee *et al.* 2021). The LDME preferentially targeted shallow-water marine species, particularly coral reef ecosystems which, prior to the extinction, covered up to 5 million square kilometres of the global oceans – roughly 10 times the surface area covered by modern reef ecosystems (Martin-Garin *et al.* 2023). Following the LDME, reef areal extent reduced by a factor of up to 5000 (McGhee *et al.* 2021). A number of reef-building species, including tabulate and rugose corals, and stromatoporoid sponges, failed to re-proliferate to pre-extinction levels (Wood 2004) and disappeared from the geological record for up to 30 Myr (Yao *et al.* 2015). Cumulatively, current estimates suggest that up to 40% of marine species went extinct by the end of the LDME (Stanley 2016).

In contrast to the mass species death within the global oceans, on land, life was flourishing. The Devonian period is now well-known as the time at which land plants first colonised the majority of Earth's land-surface, culminating in the colonisation of dry, upland continental interiors by vascular land plants, and the first developments of forest ecosystems (arborescence) (Kabanov *et al.* 2023). It is this Devonian

*Student Author
†Corresponding academic contact: Rachel.Wood@ed.ac.uk

rise of land plants that is thought to have driven one of the greatest oxygenation events in earth history (Wallace *et al.* 2017); indeed, by the early Carboniferous, atmospheric oxygen (pO_2) levels reached 21% from 10-12% in the early-Devonian, matching present-day levels (Dahl *et al.* 2010). Such connections between the rise of land plants and atmospheric oxygenation, as well as a number of global environmental changes, ultimately led Algeo *et al.* 1995 to suggest that the rise of land plants was responsible for causing the LDME when they proposed the land-plant weathering hypothesis. This hypothesis suggests that the development of arborescence and an increase in the abundance of deeply-rooting plants would increase global rates of continental chemical weathering and drive the deposition of greater volumes of nutrients (chiefly nitrogen and phosphorus) to the oceans via river systems (Algeo *et al.* 1998). Such increases in nutrient supply would enhance shallow-marine productivity, stimulating algal blooms and driving widespread surface eutrophication and, ultimately, marine anoxia, proving fatal to many marine species (Algeo *et al.* 1995).

Marine anoxia is commonly expressed in the geological record through the presence of bituminous black-shale horizons that represent an accumulation of large quantities of organic matter, preserved under anoxic surface waters (Poty *et al.* 2011; Yao *et al.* 2015). Whilst such black-shale horizons are globally ubiquitous, and have been dated to coincide with the events of the LDME (Buggisch 1972), not all shallow-marine environments are prone to developing conditions which facilitate black-shale deposition. As such, it is necessary to turn to the geochemical proxy record to assess redox conditions at this time. To do this, early marine cements, formed within reefal limestones upon early formation of the limestone itself, which have not previously been used to understand the changing seawater redox changes across the LDME, have been investigated here to deduce whether or not marine anoxia is recorded by these cements, and to assess their ability to record reliable geochemical signatures.

Methods

In order to analyse the long-term seawater chemistry changes that may have occurred across the LDME, samples of pre-extinction (Frasnian), mid-extinction (Famennian), and post-extinction (Carboniferous) -age reefal limestones were analysed from the Canning Basin in Western Australia (Frasnian and Famennian), and from Roscobie Quarry in Fife, Scotland (Carboniferous), respectively. Early marine cements within these samples have been targeted by this study where previous studies have suggested that they are reliable proxies for recording seawater chemistry because they directly precipitate from the seawater in which they form (Webb *et al.* 2000; Nothdurft *et al.* 2004; Wallace *et al.* 2017; Xiong *et al.* 2023). The rare earth element (REE) cerium (Ce), present in trace amounts within these early marine cements, was analysed to measure the oxidation state of the seawater within which the cements formed. Where other REE's, such as lanthanum (La) and neodymium (Nd) exist in trivalent oxidative states, trivalent Ce is instead converted to an insoluble tetravalent state in well-oxygenated seawater (German *et al.* 1990), and so can be used as a measure of oxidative Ce removal (Xiong *et al.* 2023) when compared to the abundance of trivalent Ce to other trivalent REE's. This relative abundance, represented through a 'cerium anomaly' (Ce_{anom}), can indicate whether the cements formed in oxygenated or anoxic seawater (Banner *et al.* 1988; Tostevin *et al.* 2016) and, as such, can inform us about the redox state of the seawater within which they precipitated. Should a Ce_{anom} be negative ($Ce_{anom} < 1$, indicating conversion of trivalent Ce to tetravalent Ce), then the early marine cements precipitated in oxygenated seawater, and where a Ce_{anom} is positive ($Ce_{anom} > 1$, indicating little to no conversion of trivalent Ce to tetravalent Ce), then the early marine cements precipitated in poorly-oxygenated or anoxic waters (Xiong *et al.* 2023).

The Ce_{anom} of early marine cements from this study are plotted through time to understand the longer-term oxygenation status of seawater before, during, and after the LDME (Figure 1) and were compared against other studies which derived their Ce_{anom} data from whole-rock data as opposed to directly targeting early marine cements.

Results

Results from this study indicate that immediately prior to the LDME, early marine cements were forming within seawater that was weakly oxygenated, with occasional interactions with at least dysoxic waters, where Frasnian Ce_{anom} values range between 0.972 and 1.121. However, during the LDME, seawater redox conditions were highly dynamic, fluctuating between strongly oxygenated and strongly anoxic waters, with Famennian Ce_{anom} values ranging between 0.203 to 1.400. Results from this study suggest

that seawaters were well-oxygenated post-extinction, with Carboniferous Ce_{anom} values ranging between 0.745 and 0.831.

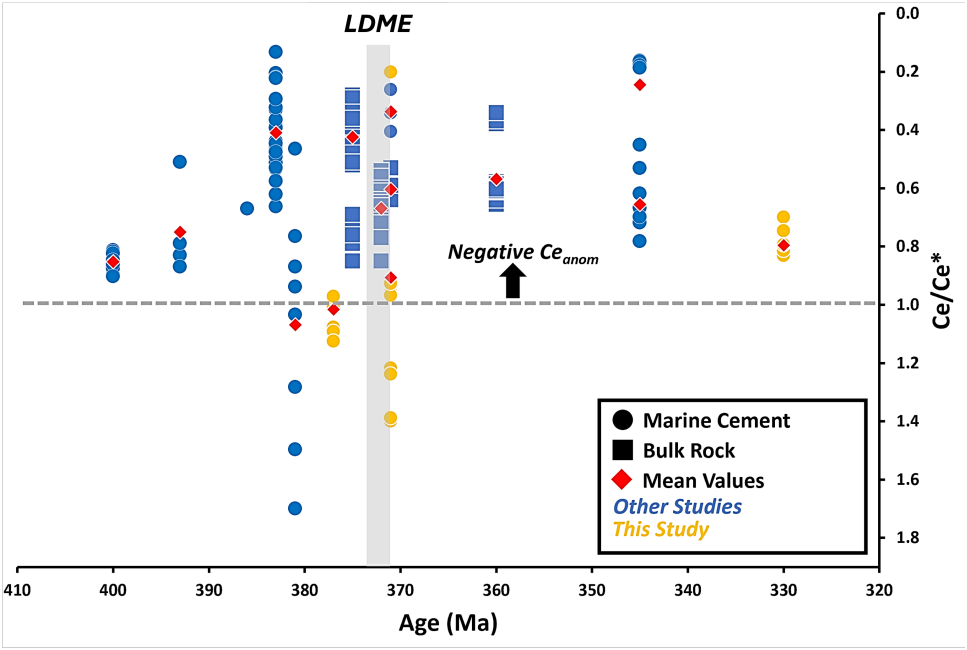

Figure 1: Plot of compiled Ce anomaly data from this study and from other studies (Nothdurft *et al.* 2004; Ma *et al.* 2008; Zeng *et al.* 2011; Franchi *et al.* 2016; Wallace *et al.* 2017; Kalvoda *et al.* 2018) displaying values for data derived from early marine cements and whole (bulk) rock data from carbonate rocks. Ce/Ce* denotes the cerium anomaly. Note that the grey shaded area marks the approximate timing of the LDME. Blue data points represent data gathered from other studies, whereas yellow data points represent data gathered from this study. Square data points indicate whole-rock data, whereas circle data points indicate early marine cement data. Mean values for each data-set included in the plot are represented by red diamonds.

The Ce_{anom} values captured in this study record the onset of anoxic conditions that continued into the LDME, which suggests marine anoxia was the primary driver of the LDME (Wallace *et al.* 2017). The fact Ce_{anom} values continue to record highly oxygenated seawaters in the Famennian suggests that the rise of land plants was responsible for driving the LDME, where the development of arborescence in the mid-Devonian drove an increase in pO_2 to levels comparable to modern-day levels by the Famennian (LDME). Famennian Ce_{anom} values also suggest that arborescence caused increased continental weathering and the transport of elevated concentrations of nutrients to the global oceans sufficient to cause shallow-marine eutrophication and mass species death (Algeo *et al.* 1995; Edwards *et al.* 2015; Wallace *et al.* 2017) as evidenced by occasional incursions of strongly anoxic seawater during the Famennian.

It should be noted that, of the studies included in Figure 1, only those studies which used early marine cements (see Ma *et al.* 2008; Wallace *et al.* 2017) were able to capture marine anoxia across the LDME. Studies which analysed whole-rock samples, without isolating early marine cements, failed to capture the true dynamic nature of seawater redox through the LDME, suggesting that greater emphasis should be placed on utilising early marine cements to analyse changing seawater chemistry.

Conclusion

This study demonstrates that the rise of land plants can likely be implicated in causing the LDME, where cerium anomalies within reefal limestone early marine cements record incursions of anoxia throughout the time of the mass extinction interval. cerium anomalies also record periods of seawater oxygenation, particularly into the lower Carboniferous, where early marine cements record only negative Ce_{anom}. Such Ce_{anom} values in the Carboniferous reflect the stabilisation of seawater redox conditions following the development of arborescence, as well as the colonisation of continental interiors, to more oxygenated conditions, following initially high nutrient inputs as a result of greatly enhanced continental weathering

during the initial stages of the development of forest ecosystems, which is itself represented in the positive Ce_{anom} values seen during both the Frasnian and Famennian periods coincident with the LDME.

Further work is needed to place the Ce_{anom} results from this study into a more robust framework in order to determine whether specific instances of marine anoxia can be dated to coincide with the five bursts of species death which characterise the LDME.

References

Algeo, T. J. *et al.* 'Late Devonian Oceanic Anoxic Events and Biotic Crises: 'Rooted' in the Evolution of Vascular Land Plants' GSA Today **5** 3 (1995)

Algeo, T. J. and Scheckler, S. E. 'Terrestrial-Marine Teleconnections in the Devonian: Links Between the Evolution of Land Plants, Weathering Processes, and Marine Anoxic Events' Philosophical Transactions of the Royal Society of London. Series B: Biological Sciences **353** 1365 (1998)

Banner, J. L. *et al.* 'Rare Earth Element and Nd Isotopic Variations in Regionally Extensive Dolomites From the Burlington-Keokuk Formation (Mississippian); Implications for REE Mobility During Carbonate Diagenesis' Journal of Sedimentary Research **58** 3 (1988)

Buggisch, W. 'Zur Geologie Und Geochemie Der Kellwasserkalke Und Ihrer Begleitenden Sedimente (Unteres Oberdevon)' (Wiesbaden; 1972)

Dahl, T. W. *et al.* 'Devonian Rise in Atmospheric Oxygen Correlated to the Radiations of Terrestrial Plants and Large Predatory Fish' Proceedings of the National Academy of Sciences **107** 42 (2010)

Edwards, D. *et al.* 'Could Land-Based Early Photosynthesizing Ecosystems Have Bioengineered the Planet in Mid-palaeozoic Times?' Palaeontology **58** 5 (2015)

Franchi, F. *et al.* 'Trace Elements and REE Geochemistry of Middle Devonian Carbonate Mounds (Maïder Basin, Eastern Anti-atlas, Morocco): Implications for Early Diagenetic Processes' Sedimentary Geology **343** (2016)

German, C. R. and Elderfield, H. 'Application of the Ce Anomaly as a Paleoredox Indicator: The Ground Rules' Paleoceanography **5** 5 (1990)

Kabanov, P. *et al.* 'Oceanic Anoxic Events, Marine Photic-Zone Euxinia, and Controversy of Sea-Level Fluctuations During the Middle-Late Devonian' Earth-Science Reviews **241** (2023)

Kalvoda, J. *et al.* 'Fine-Scale LA-ICP-MS Study of Redox Oscillations and REEY Cycling During the Latest Devonian Hangenberg Crisis (Moravian Karst, Czech Republic)' Palaeogeography, Palaeoclimatology, Palaeoecology **493** (2018)

Ma, X. P. *et al.* 'Facies and Geochemistry Across the Early-Middle Frasnian Transition (Late Devonian) on South China Carbonate Shelf: Comparison With the Polish Reference Succession' Palaeogeography, Palaeoclimatology, Palaeoecology **269** 3 (2008)

Martin-Garin, B. and Montaggioni, L. F. 'The Highs and Lows of the Reef Phenomenon' in Corals and Reefs: From the Beginning to an Uncertain Future (Springer International Publishing; 2023)

McGhee, G. R. and Racki, G 'Extinction: Late Devonian Mass Extinction' (Wiley; 2021)

Nothdurft, L. D. *et al.* 'Rare Earth Element Geochemistry of Late Devonian Reefal Carbonates, Canning Basin, Western Australia: Confirmation of a Seawater REE Proxy in Ancient Limestones' Geochimica et Cosmochimica Acta **68** 2 (2004)

Poty, E *et al.* 'Bio- and Sequence Stratigraphic Correlations Between Western Europe and South China: To a Global Model of the Eustatic Variations During the Mississippian' in Programme and Abstracts: The XVII International Congress on the Carboniferous and Permian (Geological Survey of Western Australia; 2011)

Racki, G. 'Big 5 Mass Extinctions' in Encyclopedia of Geology (Elsevier; 2021)

Raup, D. M. and Sepkoski, J. J. 'Mass Extinctions in the Marine Fossil Record' Science **215** 4539 (1982)

Stanley, S. M. 'Estimates of the Magnitudes of Major Marine Mass Extinctions in Earth History' Proceedings of the National Academy of Sciences **113** 42 (2016)

Tostevin, R. *et al.* 'Effective Use of Cerium Anomalies as a Redox Proxy in Carbonate-Dominated Marine Settings' Chemical Geology **438** (2016)

Wallace, M. W. *et al.* 'Oxygenation History of the Neoproterozoic to Early Phanerozoic and the Rise of Land Plants' Earth and Planetary Science Letters **466** (2017)

Webb, G. E. and Kamber, B. S. 'Rare Earth Elements in Holocene Reefal Microbialites: A New Shallow Seawater Proxy' Geochimica et Cosmochimica Acta **64** 9 (2000)

Wood, R. 'Palaeoecology of a Post-extinction Reef: Famennian (Late Devonian) of the Canning Basin, North-Western Australia' Palaeontology **47** 2 (2004)

Xiong, Y. *et al.* 'The Record of Sea Water Chemistry Evolution During the Ediacaran-Cambrian From Early Marine Cements' The Depositional Record **9** 3 (2023)

Yao, L. *et al.* 'The TICE Event: Perturbation of Carbon-Nitrogen Cycles During the Mid-tournaisian (Early Carboniferous) Greenhouse-Icehouse Transition' Chemical Geology **401** (2015)

Zeng, J. *et al.* 'Hydrothermal Activities and Seawater Acidification in the Late Devonian FF Transition: Evidence From Geochemistry of Rare Earth Elements' Science China Earth Sciences **54** 4 (2011)

Journal Acknowledgements

My sincere thanks to all those who helped during the process of creating and publishing the journal. In addition to the editorial board and editorial team listed at the start of this issue, I would also like to thank the Edinburgh Diamond team, in particular Rebecca Wojturska, as well as Ben Fisher, for their support and guidance in the publication of this issue.

Jack L Smith, Editor-in-Chief